Thermal Science and Engineering Progress 46 (2023) 102171

Contents lists available at ScienceDirect

Thermal Science and Engineering Progress

journal homepage: www.sciencedirect.com/journal/thermal-science-and-engineering-progress

Numerical modeling of flashing in TFC expanders for the efficient exploitation of low-grade heat

Anastasios Skiadopoulos [a,*], George Kosmadakis [b], Steven Lecompte [c], Michel De Paepe [c], Dimitrios Manolakos [a]

[a] Agricultural University of Athens, Dept. of Natural Resources Management and Agricultural Engineering, Athens, Greece
[b] Ricreation IKE, Technological Park "Lefkippos", Patriarchou Grigoriou & Neapoleos 27, 15341 Agia Paraskevi, Greece
[c] Ghent University, Department of Electromechanical, Systems and Metal Engineering, Ghent, Belgium

ARTICLE INFO

Keywords:
Two-phase expansion
Thermodynamic model
Twin-screw expander
TFC
Low-grade heat recovery

ABSTRACT

This paper presents a novel semi-empirical thermodynamic model for the simulation of two-phase expansion in twin-screw expanders. The model utilizes a limited number of unknown parameters, the values of which are calculated through a calibration-optimization process that exploits numerical experiments available in the literature. Two-phase expansion simulations are performed for a wide variety of operating conditions, revealing that the vapor quality at the suction port of the expander is the main factor affecting its efficiency. Increased vapor qualities at the onset of expansion lead to an increase in the expander's efficiency because a better matching between the WF's volume ratio and the expander's built-in volume ratio can be achieved. The thermodynamic model is applied to assess the performance of a TFC engine operating under varying heat duties and temperatures of the heat source, indicating that a detailed analysis is necessary to conclude whether the TFC or the ORC is the optimal solution for a given application.

1. Introduction

Environmental degradation in combination with the ever-increasing energy demand set unprecedented challenges for policymakers and engineers. The European Council recently adopted the "2030 Climate and Energy Framework" [1] to accelerate the pace toward a sustainable and climate-neutral economy. The policies in this framework set as key targets the drastic reduction of greenhouse gas emissions, the significant increase in the share of renewable energy sources in the energy mixture (at least 32 %), and the amelioration of the primary energy conversion efficiency (by at least 32.5 %) by 2030.

Primary energy conversion efficiency can be substantially increased by exploiting the waste heat from industrial processes. It is estimated that, globally, about 72 % of primary energy is lost in the form of waste heat during the conversion process [2]. Annually, waste heat is estimated to be in the order of 68 PWh on a global scale, roughly categorized into low-temperature heat (<100 °C), medium-temperature heat (100–300 °C), and high-temperature heat (HTH), with respective shares equal to 63 %, 16 %, and 21 % [2] (similar shares are estimated in the European Union [3]). Efficient and robust technological solutions for the exploitation of medium and low-temperature waste heat can also be directly applied for solar energy (collected in temperatures < 150 °C) exploitation, increasing, thus, the share of renewable energy sources in the overall energy mix.

Waste heat can be recovered by utilizing a bottoming thermodynamic power cycle, with the most common solutions being the Brayton Cycle, the Stirling Cycle, the Organic Rankine Cycle (ORC), the Kalina Cycle, and the Carbon Dioxide Trans-Critical Cycle. The ORC is identified as the most robust alternative for the conversion of low-grade heat because of its adaptability, scalability, and low maintenance cost [4]. The efficiency amelioration of the ORC is an issue that has attracted intense research interest (e.g. [5–8]), with the increased exergy destruction of the heat source during the heat transfer to the Working Fluid (WF), resulting in reduced power generation, identified as a main disadvantage of the power cycle. The exergy of the heat source is mainly destroyed during the evaporation of the WF, because its temperature remains constant while heat is supplied to it from a source that is cooled down, leading to a sub-optimal temperature match between the WF and the heat source [7]. Theoretical thermodynamic analysis concludes that the optimal variation of the traditional ORC, in terms of exergy destruction minimization, is a power cycle resembling a triangular shape

* Corresponding author.
E-mail address: tskiado@aua.gr (A. Skiadopoulos).

https://doi.org/10.1016/j.tsep.2023.102171
Received 20 September 2022; Received in revised form 28 August 2023; Accepted 1 October 2023
Available online 2 October 2023

Nomenclature

p	Pressure [bar]
T	Temperature [^{o}C]
h	Specific enthalpy [kJ/kg]
s	Specific entropy [kJ/kg-K]
v	Specific volume [m^3/kg]
x	Vapor quality [-]
c_p	Specific heat [kJ/kg-K]
$\dot{m}$	Mass flow rate [kg/s]
$\dot{X}$	Exergy flow [kW]
$\dot{w}$	Power [kW]
$\dot{Q}$	Heat transfer rate [kW]
r_v	Expander built-in volume ratio [-]
N	Expansion sub-chambers [-]
N_P	Model calibration points [-]
N_{rot}	Rotational speed [rpm]
A	Area [m^2]
UA	Thermal conductance [W/K]
V_{swept}	Swept volume [m^3]
V	Expansion chamber volume [m^3]

Subscripts

in	Inlet
su	Suction
sh	Shaft
is	Isentropic
ex	Expander
exp	Expansion
ev	Evaporator
con	Condenser
out	Outlet
sub	Sub-cooling
pr	Pre-heating
pu	Pump
sat	Saturated
th	Thermal
0	Dead state
II	Second law
l	Liquid
v	Vapor
leak	*Leakages*
si	Simulation
cb	Calibration point
thr	Nozzle throat
crit	Critical
w	Wall
no	Nominal
dis	Discharge
pc	Post vaporization
amb	Ambient
f	Flashing

Greek letters

ψ	Specific exergy[kJ/kg]
η	Efficiency [-]
γ	Specific heat ratio [-]
τ	Mechanical torque [N-m]

Abbreviations

PP	Pinch point temperature difference [^{o}C]
HTF	Heat Transfer Fluid
CF	Cooling Fluid
WF	Working Fluid
TFC	Trilateral Flash Cycle
ORC	Organic Rankine Cycle

[6,7,9], in a configuration where the evaporation of the WF is avoided.

A power cycle approaching the ideal triangular shape is the Trilateral Flash Cycle (TFC). A TFC engine has the same components as the ORC, but the WF enters the expansion machine as a saturated liquid (in the original concept) or partially evaporated two-phase mixture (in a generalization of the trilateral cycle concept), where it undergoes two-phase expansion, also referred to as flashing. The TFC was originally conceived by Smith et al. [10] for heat recovery in geothermal applications. In this reference work, the authors performed a comparison between the standard ORC, the supercritical ORC, and the TFC, with the heat source temperature between 100 and 200 °C, concluding that the TFC outperforms all other architectures, in terms of net power maximization, for all screened WFs. Despite its acknowledged potential, though, the TFC has not been widely applied for low-grade heat recovery, with the development of efficient and robust two-phase expansion machines being the main technological bottleneck. This is because the evolution of flashing in expansion machines is not comprehended sufficiently. The main challenge that must be overcome is the prediction of the vaporization rate of the WF in the expander since the two phases are in thermodynamic non-equilibrium throughout the process, i.e. their pressure and temperature are different.

Only a few experimental studies concerning two-phase expansion have been published so far. Mckay and Sprankle [11] were the first to perform flashing experiments for geothermal energy recovery, with H_2O as the WF in a 1 MW turbine. The authors conducted experiments with vapor qualities in the range of 0–99 %, reporting turbine adiabatic efficiencies up to 62 %. Steidel et al. [12] conducted experimental laboratory tests with geothermal fluids undergoing two-phase expansion in twin-screw expanders. They were able to achieve maximum adiabatic efficiency in the order of 53 % for initial vapor qualities of the WF in the range of 8 % to 27 %. Smith et al. [13] performed extensive experimental studies of two-phase expansion in different twin-screw expanders with H_2O and R113 as WFs. They were able to achieve maximum expander adiabatic efficiencies in the order of 80 %. Kliem [14] used twin-screw expanders with specially designed filling systems to perform two-phase expansion experiments with H_2O as the WF. He achieved adiabatic efficiencies up to 50 %. Öhman and Lundqvist [15] tested a semi-hermetic Lysholm turbine with R134a as a WF for variable inlet vapor qualities, achieving maximum adiabatic efficiency in the order of 92 %. Lastly, Kanno and Shikazono [16] studied experimentally two-phase expansion in a reciprocating cylinder that simulated the operation of a piston expander. They used H_2O and ethanol as WFs, and they calculated maximum adiabatic efficiencies equal to 86 % and 82 %, respectively.

Concerning numerical modeling, many simulations of the TFC have been performed but, in most cases, the two-phase expander is treated as a black box, and its adiabatic efficiency is varied within the range of values achieved by expanders in the dry vapor region to investigate its effect on the efficiency of the power cycle (e.g.[5,8,17,18]). Only a few efforts have been undertaken to numerically model the flashing phenomenon in an expansion machine. To the best of the authors' knowledge, there are, up until now, no full 3-D Computational Fluid Dynamics studying flashing in industrial expanders. On the other hand, a few lower-order models simulating flashing are documented in the literature. All the published low-order models simulate two-phase expansion in twin-screw expanders. Taniguchi et al. [19], and Smith et al. [13] developed analytical 1-D models for the simulation of two-phase expansion that solve the conservation equations for the vapor–liquid

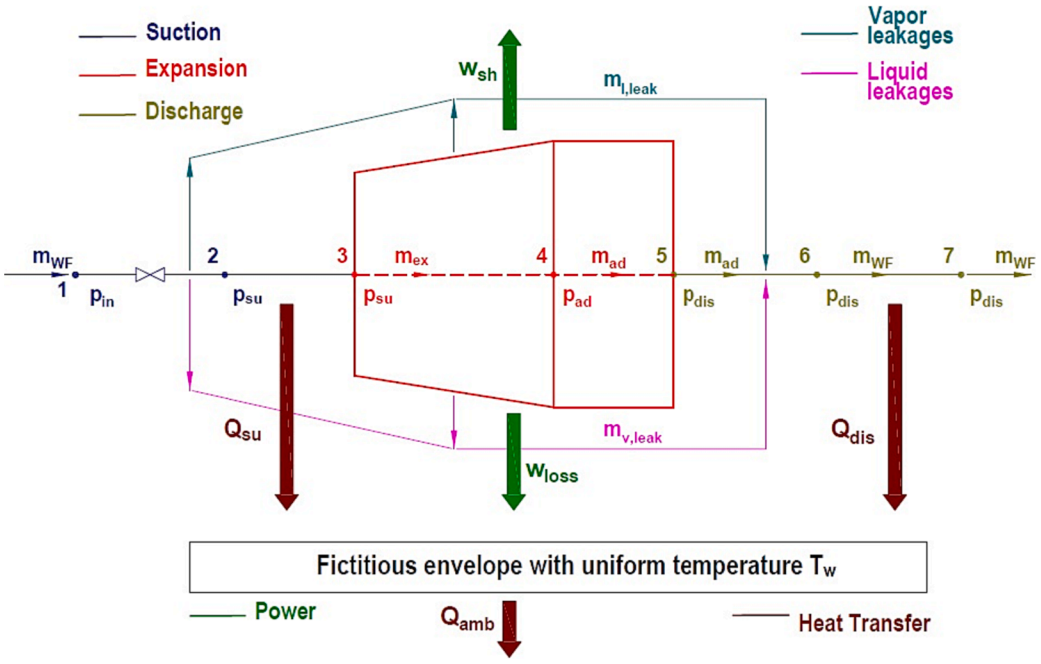

Fig. 1. Two-phase expansion model concept.

mixture, which is treated as a single-fluid. The thermodynamic properties of the mixture are correlated by applying an equation of state, and the two distinct phases are assumed to be in thermodynamic equilibrium. A 1-D thermodynamic model was developed by Vasuthevan and Brümmer [20] for the numerical modeling of flashing in a representative twin-screw expander geometry, with H_2O as the WF. In this work, two series of simulations were performed for comparison reasons. In the first, the WF was assumed to be in thermodynamic equilibrium throughout flashing, whereas in the second non-equilibrium effects were considered by applying the flashing efficiency formula introduced by Miyatake et al. [21]. Finally, Bianchi et al. [22] modeled flashing by utilizing the commercial software suite GT-SUITE. This model is also 1-D, and the two-phase mixture is treated as a single fluid.

The current work presents a semi-empirical low-order thermodynamic model for the simulation of two-phase expansion in an oil-free twin-screw expander. The model aims to serve as a robust tool for the industrial and research communities in the design of efficient two-phase expanders and performance evaluation of TFC engines. The approach is based on the well-established methodology presented by Lemort et al. [23], adapted and substantially appended for the simulation of the complex flashing phenomenon. To the best of the authors' knowledge, the current work presents the first semi-empirical thermodynamic model for the simulation of two-phase expansion. The model can simulate two-phase expansion for varying vapor quality at the suction port of the expander by utilizing only a set of parameters that are calculated by solving a properly formulated optimization problem. A prominent feature of the model is that vapor and liquid are treated as different fluids, and the conservation equations are formulated separately for each phase. During flashing the two phases are considered to be in thermal non-equilibrium, and the WF vaporization rate is determined by estimating the heat transfer rate at their interface. Furthermore, a segmental approach is applied in the expansion chamber, allowing for the detailed monitoring of the vaporization rate as flashing evolves. Only minor inputs concerning the geometrical characteristics of the expander are necessary, a feature particularly useful when detailed constructional data are not available by manufacturers.

In the remainder of this work, initially, the modeling methodology applied for the simulation of two-phase expansion is presented. Thereafter, the methodology for integrating the two-phase expansion model into a TFC simulation tool is described. In the second part of the paper, the calibration–validation procedure of the two-phase expansion model is initially presented. The values of the identified parameters are calculated by solving properly formulated optimization problems and, subsequently, the obtained numerical results are compared to the simulations presented by Bianchi et al. [22] for an industrial twin-screw expander. Next, the performance of the two-phase expander for a wide variety of operating conditions is mapped to identify the main factors affecting its efficiency. Finally, the performance of a TFC engine integrating the modeled two-phase expander is investigated, under varying heat duties at the evaporator, temperatures of the heat source, and vapor qualities at the suction port of the expander. This investigation demonstrates how the performance of the two-phase expander, for different vapor qualities of the WF at the suction port, affects the overall heat recovery efficiency. The results are exploited to determine the optimal operating point of the engine, and, also, to assess whether, based on the anticipated operating conditions, the TFC or the standard ORC may be a better alternative.

2. Two-phase expansion modeling

2.1. Modeling concept outline

The developed two-phase expansion model is a single-chamber one. Hence, the interactions between actual adjacent working chambers, created by the expander's meshing lobes, are not taken into account and the properties of the WF are an average value at the examined operational phase of the expander, which is determined by the rotational angle of the male lobe. The conservation equations are solved separately for the liquid and vapor phases between successive male rotor angles. The coupling of the conservation equations of the two phases is accomplished by the heat transfer rate at the vapor–liquid interface, which determines the WF vaporization rate. This rate is constantly monitored from the suction port (pre-expansion of the WF) to the discharge port. Several approaches, with different levels of complexity, have been proposed in the literature for the numerical modeling of the vaporization rate of a pure substance, such as the Homogenous Equilibrium Model [24], the Homogenous Relaxation Model [25], the Bubble Growth Model [26], and the Interfacial Exchange Model [26]. In the

Table 1
Boundary conditions and outputs for two-phase expansion simulations.

Boundary Conditions	
Symbol	**Description [Units]**
x_{in}	Quality of the WF at the suction port of the expander [-]
p_{in}	Pressure at the suction port [bar]
p_{dis}	Pressure at the discharge line [bar]
N_{rot}	Rotational speed of the expander [rpm]
Outputs	
Symbol	**Description [Units]**
$\dot{m}_{WF}$	Mass flow rate of the WF [kg/s]
$\dot{w}_{sh}$ [kW]	Expander shaft power [kW]

present work, the Interfacial Exchange Model has been applied because of its generality, ease of implementation in different applications, and the fact that it can straightforwardly take into consideration non-equilibrium effects. Another prominent feature of this work is that leakage flows are accounted separately for the two phases at the suction port and the expansion chamber. The fundamental modeling assumptions applied for the model development are the following.

- The operation of the expander has reached steady-state
- The two phases are in mechanical equilibrium but thermal non-equilibrium
- Vapor at the vapor–liquid interface is saturated during two-phase expansion [26]
- Work is generated only by the expansion of the locally available vapor
- Heat losses of the WF are considered only during suction and discharge [23]
- Heat losses from saturated vapor are not taken into account

The complete description of the developed two-phase expansion model is presented in Appendix A in detail. The model presentation consists of the methodology and governing equations, along with the identified set of unknown parameters. The developed model encompasses all the thermodynamic processes that take place in the general case of two-phase expansion in a twin-screw expander. According to the physical problem studied, simplifications may arise leading to a reduced set of unknown parameters. A conceptual scheme of the two-phase expansion model is presented in Fig. 1. The illustrated concept depicts the thermodynamic processes that take place in the general case of flashing in a twin-screw expander (details on the determination of the vaporization rate and leakage flows are given in detail in Appendix A). These processes, grouped according to the operational phase of the expander, are:

1) **Suction**
a) Adiabatic supply pressure drop from pressure p_{in} to p_{su} (1 → 2), followed by leakage flows from both phases toward the discharge port
b) Isobaric cooling down of the WF at pressure p_{su} (2 → 3)
2) **Expansion**
   a) Adiabatic expansion to the pressure p_{ad} imposed by the built-in volume ratio
   b) r_v of the expander (3 → 4). A segmental approach is followed, and, based on
   c) r_v, the expansion chamber volume is divided into N segments to accurately monitor the evolution of the flashing phenomenon. Leakage flow rates from both phases toward the discharge port are calculated at each segment.
   d) Adiabatic and isochoric expansion to the discharge pressure p_{dis} (4 → 5)
3) **Discharge**
a) Adiabatic mixing between leakage flow rates (both vapor and liquid) from suction and expansion and two-phase mixture flowing out of the expansion chamber (5 → 6)
b) Isobaric heat transfer from the two-phase mixture towards the expander wall at pressure p_{dis} (6 → 7)

The numerical algorithm is formulated in the Engineering Equations Solver software suite (v10.834). The system of governing equations of the two-phase expansion model (details in Appendix A) is solved iteratively until convergence (relative residuals drop below 10^{-6} for all equations).

2.2. Boundary conditions and outputs

The boundary conditions and outputs for the two-phase expansion simulations, along with their description and units are listed in Table 1. Alternatively, $\dot{m}_{WF}$ can be imposed as a boundary condition, in which case p_{in} would be an output.

In all performed numerical experiments presented herein, R245fa is the WF, to comply with the simulations presented by Bianchi et al. [22], based on which the model has been calibrated (details in Section 4.1).

2.3. Two-phase expander efficiency

The performance of the two-phase expander is quantified by its isentropic and volumetric efficiency. The isentropic efficiency $\eta_{ex,is}$ is given by Eq. (1)

$$\eta_{ex,is} = \frac{\dot{w}_{sh}}{\dot{w}_{ex,is}} \tag{1}$$

where $\dot{w}_{ex,is}$ stands for the power generated under an isentropic expansion of the WF from the suction port to the discharge pressure. The volumetric efficiency η_{vol} is given by Eq. (2)

$$\eta_{vol} = \frac{\dot{m}_{WF} v_{in}}{N_{rot} V_{swept}} \tag{2}$$

where v_{in} is the specific volume of the WF at the onset of the suction process, and V_{swept} the total swept volume.

3. TFC modeling

3.1. Thermodynamic model

In the present work, the term TFC is assumed to incorporate the power cycle configurations with the quality x_{in} of the WF at the suction port of the expander varying between 0 and 1. A thermodynamic model integrating the developed two-phase expansion model is developed for the simulation of the TFC. The integration of the two-phase expansion model will highlight the effect of the expander's efficiency on the performance of the TFC for different operating conditions. An indicative T-s diagram of the TFC power cycle with R245fa as the WF is presented in Fig. 2, with the processes undergone by the Heat Transfer Fluid (HTF) and the Cooling Fluid (CF) also drawn qualitatively.

The TFC is comprised of the following thermodynamic processes of the WF:

- 1 → 2: Adiabatic pumping
- 2 → 3: Heat absorption in the evaporator at constant pressure p_{ev}
- 3 → 4: Expansion in the twin-screw expander
- 4 → 1: Heat rejection in the condenser at constant pressure p_{con}

As the TFC engine operates, the temperature of the HTF at the evaporator drops from $T_{HTF,in}$ to $T_{HTF,out}$, whereas the temperature of the CF rises from $T_{CF,in}$ to $T_{CF,out}$. To avoid possible adverse effects from the occurrence of cavitation, the WF is assumed to be subcooled by ΔT_{sub} at

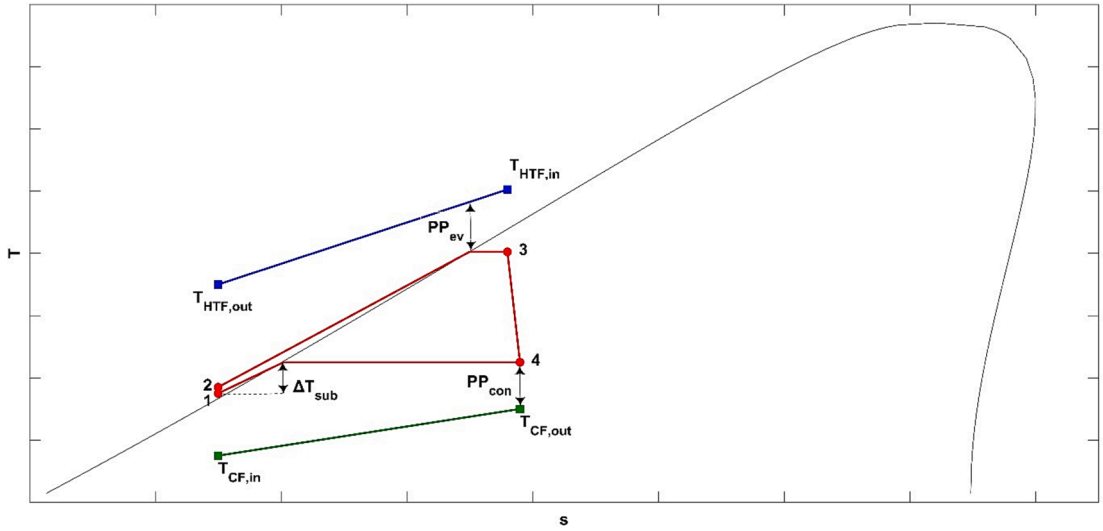

Fig. 2. T-s diagram of TFC with R245fa as WF.

the suction of the pump.

The total heat transfer rate $\dot{Q}_{ev}$ at the HTF side of the evaporator is given by Eq. (3)

$$\dot{Q}_{ev} = \dot{m}_{HTF} c_{p,HTF} \left(T_{HTF,in} - T_{HTF,out}\right) \tag{3}$$

where $\dot{m}_{HTF}$ is the mass flow rate of the HTF, and $c_{p,HTF}$ is its specific heat under constant pressure. If heat losses at the evaporator are neglected, $\dot{Q}_{ev}$ is also equal to the heat transferred to the WF, as in Eq. (4)

$$\dot{Q}_{ev} = \dot{m}_{WF}(h_3 - h_2) \tag{4}$$

where h_2 and h_3 denote its specific enthalpy at states 2, and 3, respectively. The pinch point temperature difference PP_{ev} between the fluid streams at the evaporator is given by Eq. (5)

$$PP_{ev} = T_{HTF,pr} - T_{WF,sat}(p_{ev}) \tag{5}$$

where $T_{HTF,pr}$ is the temperature of the HTF at the evaporator at the end of the WF preheating stage, and $T_{WF,sat}(p_{ev})$ is the saturation temperature of the WF at pressure p_{ev}. In the present work, a constant value of PP_{ev}, for comparison purposes between different configurations, is assumed for all vapor qualities x_{in} at the suction port of the two-phase expander. The optimal theoretical matching between the HTF and the WF at the evaporator occurs when the power cycle assumes the shape of the trilateral cycle, in which case the vaporization of the WF is omitted, and $T_{HTF,pr}$ becomes equal to $T_{HTF,in}$. It must be noted here that the location of PP_{ev} could, in the general case, be located in a different stage of the heat transfer process at the evaporator, especially when the HTF flow rate is greatly reduced, leading to a much higher difference between $T_{HTF,in}$ and $T_{HTF,out}$. However, for this work, it was assumed that it is always at the end of the WF preheating stage because this pinch point location is typical in ORC modeling, and it has been a starting point of the thermodynamic analysis to identify alternative power cycle architectures that increase thermal efficiency (an analysis that led to the conceptualization of the TFC).

Assuming a counter-flow arrangement between streams at the evaporator, the heat transfer rate $\dot{Q}_{pr}$ to the WF during the preheating stage is given by Eq. (6)

$$\dot{Q}_{pr} = \dot{m}_{HTF} c_{p,HTF} \left(T_{HTF,pr} - T_{HTF,out}\right) = \dot{m}_{WF} \left(h_{l,sat}(p_{ev}) - h_2\right) \tag{6}$$

where $h_{l,sat}(p_{ev})$ is the specific enthalpy of the WF at the saturated liquid state at p_{ev}. For a given value of p_{ev}, and a fixed value of PP_{ev}, $T_{HTF,pr}$ is calculated by Eq. (5), leading to the determination of $\dot{m}_{WF}$ from Eq. (6).

The integration of the two-phase expansion model with the thermodynamic model of the TFC is accomplished as described next. As a starting point, the desired quality x_{in} is selected. For this value of x_{in}, and given values of $\dot{Q}_{ev}$, p_{con}, PP_{ev}, and $T_{HTF,in}$, p_{ev} and N_{rot} are varied iteratively until the output mass flowrate $\dot{m}_{wf}$ of the two-phase expansion model becomes equal to the value calculated by Eq. (6), and, at the same time, Eq. (4) is satisfied.

The shaft power $\dot{w}_{sh}$ generated by the expander is calculated by the two-phase expansion model, leading, implicitly, to the determination of $\eta_{ex,is}$ from Eq. (1), where $\dot{w}_{ex,is}$ is given by Eq. (7)

$$\dot{w}_{ex,is} = \dot{m}_{WF} \left(h_3 - h_4^{is}\right) \tag{7}$$

In Eq. (7) h_4^{is} the specific enthalpy of the WF corresponding to its isentropic expansion from p_{ev} to p_{con}.

The total power input $\dot{w}_{pu}$ to the pump is calculated by applying Eq. (8)

$$\dot{w}_{pu} = \dot{m}_{WF}(h_2 - h_1) = \dot{m}_{WF} \frac{\left(h_2^{is} - h_1\right)}{\eta_{pu,is}} \tag{8}$$

In Eq. (8) h_2^{is} is the specific enthalpy of the WF corresponding to its isentropic pumping from p_{con} to p_{ev}, $\eta_{pu,is}$ is the pump's isentropic efficiency, whereas h_1 and h_2 are the specific enthalpies of the WF at states 1 and 2, respectively. The heat transfer rate $\dot{Q}_{con}$ from the WF to the CF at the condenser is given by Eq. (9)

$$\dot{Q}_{con} = \dot{m}_{WF}(h_4 - h_1) \tag{9}$$

Assuming negligible heat losses at the condenser, $\dot{Q}_{con}$ is also given by Eq. (10)

$$\dot{Q}_{con} = \dot{m}_{CF} c_{p,CF} \Delta T_{CF} \tag{10}$$

where $\dot{m}_{CF}$ and $c_{p,CF}$ are the mass flow rate and the specific heat under constant pressure of the CF, respectively, whereas ΔT_{CF} is the temperature rise of the CF at the cooling loop of the condenser. In the present work, a constant pinch point temperature difference PP_{con} at the condenser is also assumed, given by Eq. (11)

$$PP_{con} = T_{WF,sat}(p_{con}) - T_{CF,out} \tag{11}$$

with $T_{WF,sat}(p_{con})$ representing the saturation temperature of the WF at pressure p_{con}.

3.2. Performance potential

The performance potential of the TFC is evaluated according to its

Table 2
Reduced set of model parameters.

Parameter	Symbol [Units]
Nozzle throat cross-sectional area at suction	A_{in} [m^2]
Nozzle throat cross-sectional area for liquid leakage flows at suction	$A_{l,su}$ [m^2]
Nozzle throat cross-sectional area for vapor leakage flows at suction	$A_{v,su}$ [m^2]
Total swept volume	V_{swept} [m3]
Nozzle throat cross-sectional area for liquid leakage flows during expansion	$A_{l,leak}$ [m^2]
Nozzle throat cross-sectional area for vapor leakage flows during expansion	$A_{v,leak}$ [m^2]

Table 3
Optimized values of model parameters.

Parameter	Value
A_{in}	$5.022{\cdot}10^{-4}$ m^2
$A_{l,su}$	$4.454{\cdot}10^{-6}$ m^2
$A_{v,su}$	$5.326{\cdot}10^{-6}$ m^2
V_{swept}	$2.934{\cdot}10^{-4}$ m^3

first and second law efficiency. The thermal efficiency η_{th} of the engine is given by Eq. (12)

$$\eta_{th} = \frac{\dot{w}_{net}}{\dot{Q}_{ev}} = \frac{\dot{w}_{sh} - \dot{w}_{pu}}{\dot{Q}_{ev}} \tag{12}$$

with $\dot{w}_{net}$ the net generated power during the operation of the engine.

For a second law analysis, a dead state (p_0, T_0) must be specified. In the present study, the temperature $T_{CF,in}$ and pressure $p_{CF,in}$ of the CF at the inlet of the condenser's cooling loop are assumed to define the dead state. Considering steady-state conditions and neglecting potential and kinetic energy contributions, the specific exergy ψ of an open system is given by Eq. (13)

$$\psi = h - h_0 - T_0(s - s_0) \tag{13}$$

where h and s denote its specific enthalpy and entropy, respectively. The exergy flow of the open system is then calculated by Eq. (14)

$$\dot{X} = \dot{m}\psi \tag{14}$$

where $\dot{m}$ is its mass flow rate.

For the simulated TFC system, the only exergy input is the exergy $\dot{X}_{HTF,in}$ of the HTF at the evaporator. Thus, the second law efficiency η_{II} of the engine is given by Eq. (15)

$$\eta_{II} = \frac{\dot{w}_{net}}{\dot{X}_{HTF,in}} \tag{15}$$

4. Results and discussion

4.1. Two-phase expansion model validation

4.1.1. Model validation

The modeling approach applied herein for the simulation of two-phase expansion is validated by a calibration-comparison procedure, common for all semi-empirical low-order models. Calibration consists of two successive steps. Initially, the subset of the generalized model parameters (presented in Appendix A in detail) that comply with the operation of the expander in the dataset that has been selected for the calibration procedure is identified. Thereafter, these identified parameters are calculated by solving a properly formulated optimization problem, aiming to fit numerical results from the two-phase expansion model to the original dataset of operating points, which may be numerical or experimental. Following calibration, the numerical results from the two-phase expansion model are compared to the original available expander operational data to assess the overall agreement.

In the present work, the two-phase expansion model is calibrated by utilizing the numerical results presented in the work of Bianchi et al. [22] for an industrial twin-screw expander with R245fa as the WF. The calibration procedure presented herein may be performed anew for different expanders and operating conditions. It must be noted that it is of particular importance to calibrate the model with experimental data, a process that will be performed when comprehensive results from experiments become available. In the two-phase expansion simulations presented by Bianchi et al. [22], the operation of the expander was considered adiabatic, no mechanical losses were taken into account, and r_v is an input (obtaining a value of 5). The model parameters that are relevant to the operation of the specific twin-screw expander are listed in Table 2.

The calibration-optimization process of the numerical model is described next. A sufficient number N_p of two-phase expander operating points from the simulations of Bianchi et al. [22], across the widest possible range, is selected for calibration. For the selected operating points, the values for the boundary conditions and outputs (Table 1), necessary for running the two-phase expansion model, are recorded. Thereafter, initial guess values are assigned to the reduced set of model parameters (Table 2), and these values are iteratively modified, by an optimization algorithm, targeting to minimize the objective function f_{err}, calculated by Eq. (16).

$$f_{err} = \frac{1}{2}\sum_{j=1}^{N_p}\left(\frac{\dot{w}_{sh,si,j} - \dot{w}_{sh,cb,j}}{\dot{w}_{sh,cb,j}}\right)^2 + \frac{1}{2}\sum_{j=1}^{N_p}\left(\frac{\dot{m}_{WF,si,j} - \dot{m}_{WF,cb,j}}{\dot{m}_{\dot{m}_{WF},cb,j}}\right)^2 \tag{16}$$

The value of f_{err} in Eq. (16) is a measure of the total deviation between the numerical results from the two-phase expansion model and the ones by Bianchi et al. [22], as it compares the difference in the values of $\dot{m}_{WF}$ and $\dot{w}_{sh}$ for all calibration points. Optimization is performed by applying a genetic algorithm, native in the Engineering Equations Solver sofrware suite, that calculates the global optimum solution. In Eq. (16) $\dot{w}_{sh,si,j}$, and $\dot{m}_{WF,si,j}$ are the shaft power and inlet mass flowrate of the WF calculated by the model at calibration point j. Likewise, $\dot{w}_{sh,cb,j}$, and $\dot{m}_{WF,cb,j}$ are the respective shaft power and mass flowrate values provided by Bianchi et al. [22] for operating point j. In the present work, the numerical formulation of the optimization problem allows for a variation of $A_{l,leak}$ and $A_{v,leak}$ as a function of x_{in} to take into account the variation of the actual available leakage paths area for the two phases as the vapor quality at suction changes. On the other hand, x_{in}-independent values are obtained for $A_{l,su}$ and $A_{v,su}$.

In the simulations performed for optimization purposes, p_{dis} was kept constant at 1.32 bar, whereas p_{in} was in the range of 5 to 10 bar [22]. Moreover, x_{in} and N_{rot} varied from 0 to 1, and 1500 to 6000 rpm, respectively. The total number of calibration points N_p is equal to 50, whereas a total of 10 expansion sub-chambers N is proven adequate to yield discretization-independent values for the model parameters. Following the calculation of model parameters, a regression analysis is performed to correlate $A_{l,leak}$ and $A_{v,leak}$ with x_{in}. This analysis indicated that third-order polynomials, given by Eqs. (17) and (18), provide the best fit between $A_{l,leak}$ and $A_{v,leak}$ and x_{in}

$$A_{v,leak} = 1.462{\cdot}10^{-5} + 2.354{\cdot}10^{-5}x_{in} - 4.352{\cdot}10^{-5}x_{in}^2 + 3.491{\cdot}10^{-5}x_{in}^3 \tag{17}$$

$$A_{l,leak} = 3.853{\cdot}10^{-5} - 2.521{\cdot}10^{-4}x_{in} + 4.913{\cdot}10^{-4}x_{in}^2 - 2.908{\cdot}10^{-4}x_{in}^3 \tag{18}$$

The remaining set of x_{in}-independent model parameters, along with their derived values, are listed in Table 3.

Concerning the comparison between the developed two-phase expansion model and the numerical model of Bianchi et al. [22], a very good overall fit is observed, indicating the validity of the modeling approach. In Fig. 3 the calculated values of $\dot{m}_{WF}$ as a function of x_{in} are

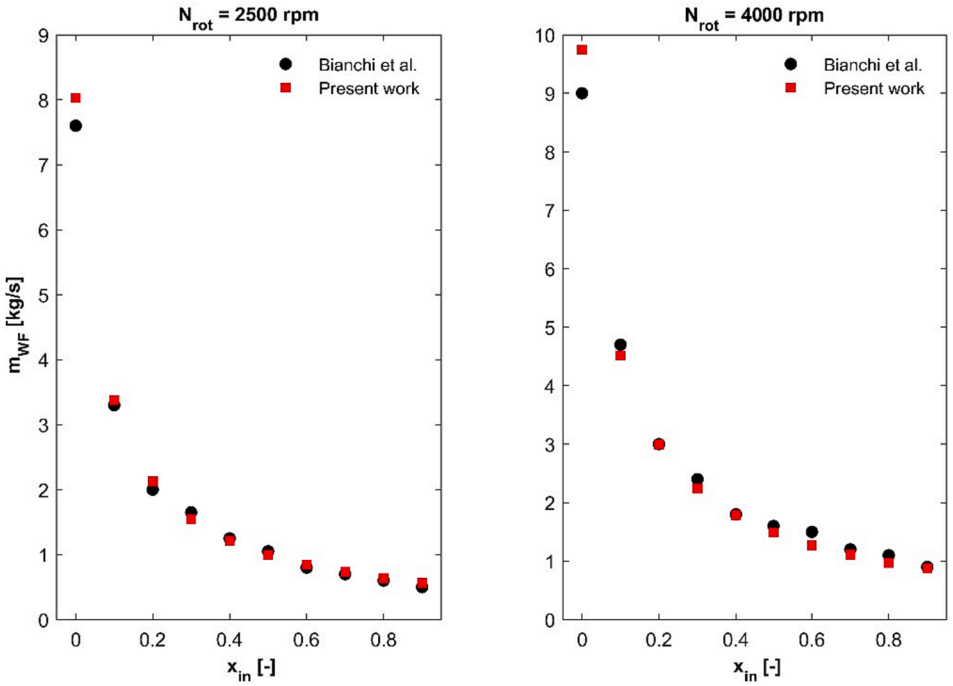

Fig. 3. Mass flow $\dot{m}_{WF}$ [kg/s] through the expander versus x_{in} for different values of N_{rot} and $p_{in} = 7.5$ bar.

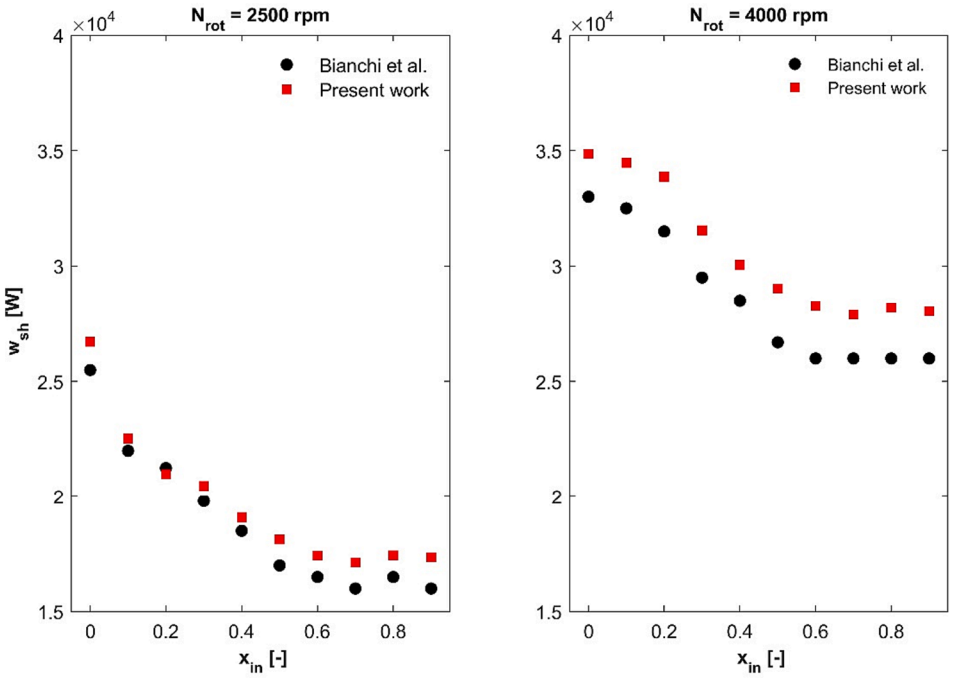

Fig. 4. Shaft power $\dot{w}_{sh}$ [W] versus x_{in} for different values of N_{rot} and $p_{in} = 7.5$ bar.

presented, indicatively, for different values of N_{rot} and $p_{in} = 7.5$ bar. A similar fit is observed for different values of p_{in}. Across the simulated operating points, a maximum relative difference of approximately 11 % in the value of $\dot{m}_{WF}$ was recorded. Differences can be linked to slight differences in the leakage path areas, since in the present work these are calculated by optimization, whereas in the original work of Bianchi et al. [22] they are available to the authors by the expander manufacturer.

In Fig. 4 calculated shaft power values $\dot{w}_{sh}$ versus x_{in} for the same operating points presented in Fig. 3 are presented. The predicted values differ by at most 9 %, compared to the reference baseline. Differences are, most likely, ought to the different modeling approaches in the case of over or under-expansion. In the present work, as is the standard practice in empirical models, an isochoric transformation is assumed to occur when the pressure at the end of expansion mismatches the one at the discharge line. On the other hand, Bianchi et al. [22] assume that this mismatch takes some crank angle degrees to develop, and they follow a modeling approach that takes into account pressure oscillations at discharge.

The results highlight that the developed two-phase expansion model can replicate with sufficient accuracy the simulations performed with a

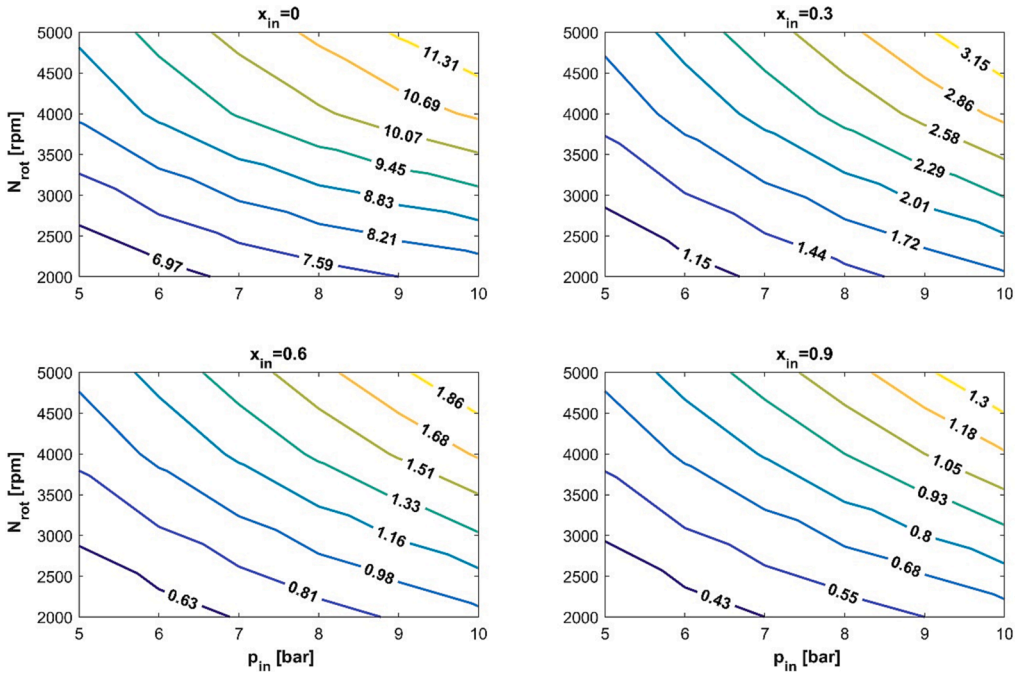

Fig. 5. Contours of $\dot{m}_{WF}$ [kg/s] as a function of N_{rot} and p_{in} for different values of x_{in}.

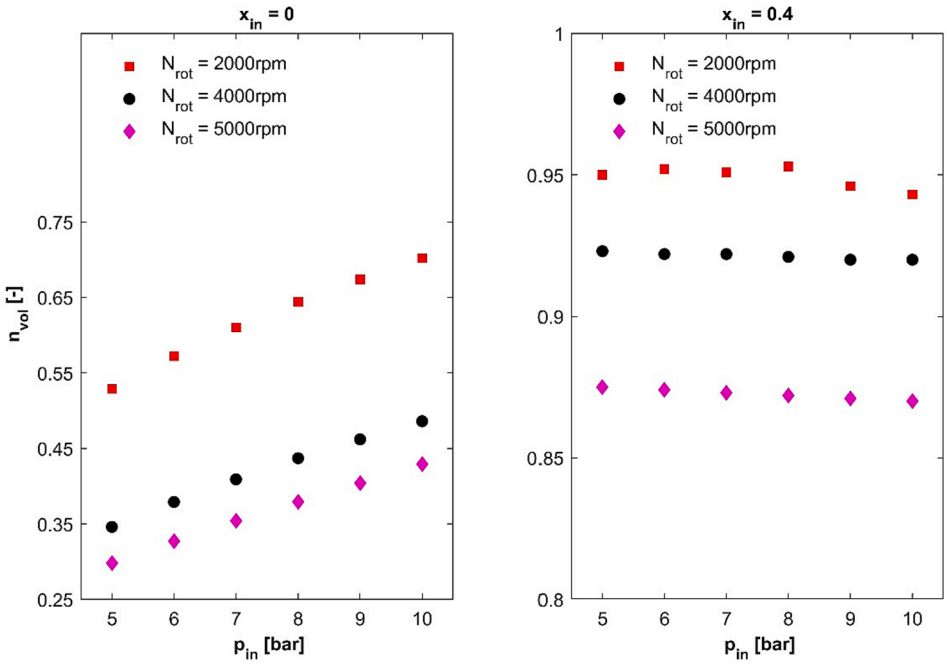

Fig. 6. η_{vol} [-] as a function of p_{in} and N_{rot} for different values of x_{in}.

robust commercial software suite (GT-SUITE) that is utilized in a wide variety of applications and industries. The modeling approach (details in Appendix A) allows for the simulation of flashing without resorting to equations of state for the two-phase mixture, the validity of which may be doubtful in non-equilibrium thermodynamics. Indeed, until now there are no equations of state valid for a substance in a metastable state [27]. This is because the spinoidal curve of the curve, i.e the thermodynamic limit beyond which minor fluctuations lead to the formation of a new phase, would have to be available. The determination of the spinoidal curve is a challenging task, and it can only be extracted experimentally for a given substance [26].

Concluding, the applied methodology allows for the simulation of the complex physical phenomenon with a high level of detail, by introducing a limited number of unknown parameters with physical significance. Moreover, the modularity of the algorithm allows for the incorporation of all physical processes that are relevant to the operation of the twin-screw expander.

4.2. Two-phase expander performance

The performance of the modeled two-phase expander (details about the expander characteristics in Section 4.1) is mapped by conducting a

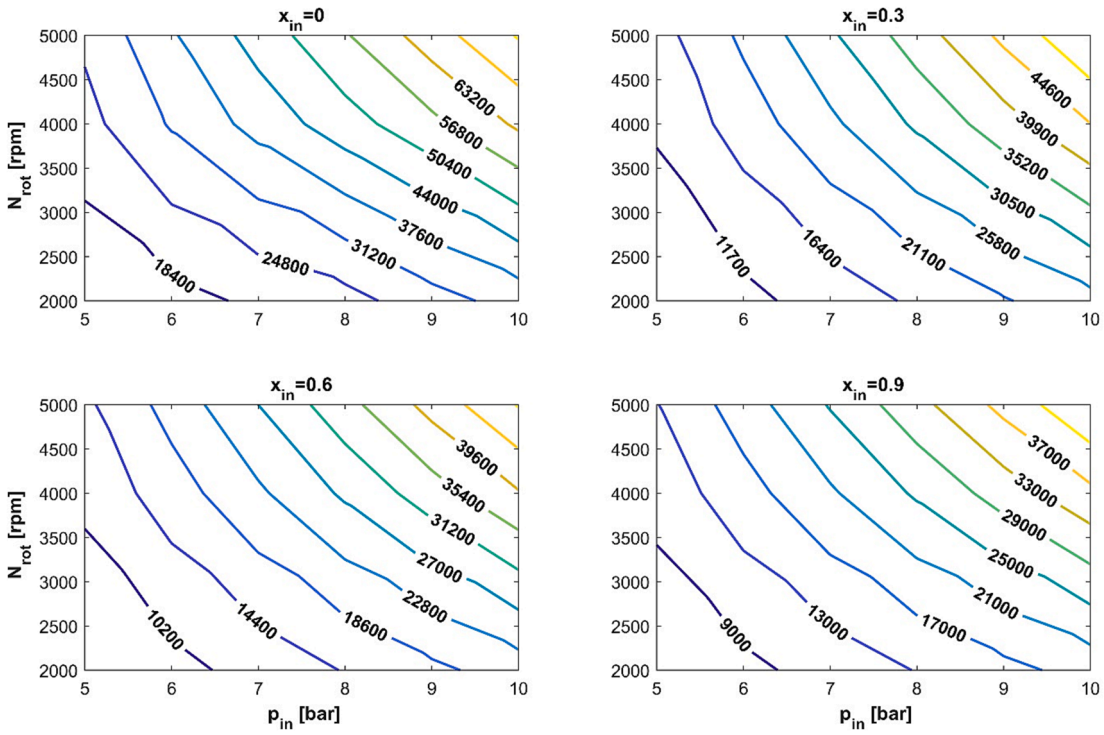

Fig. 7. Contours of $\dot{w}_{sh}$ [W] as a function of N_{rot} and p_{in} for different values of x_{in}.

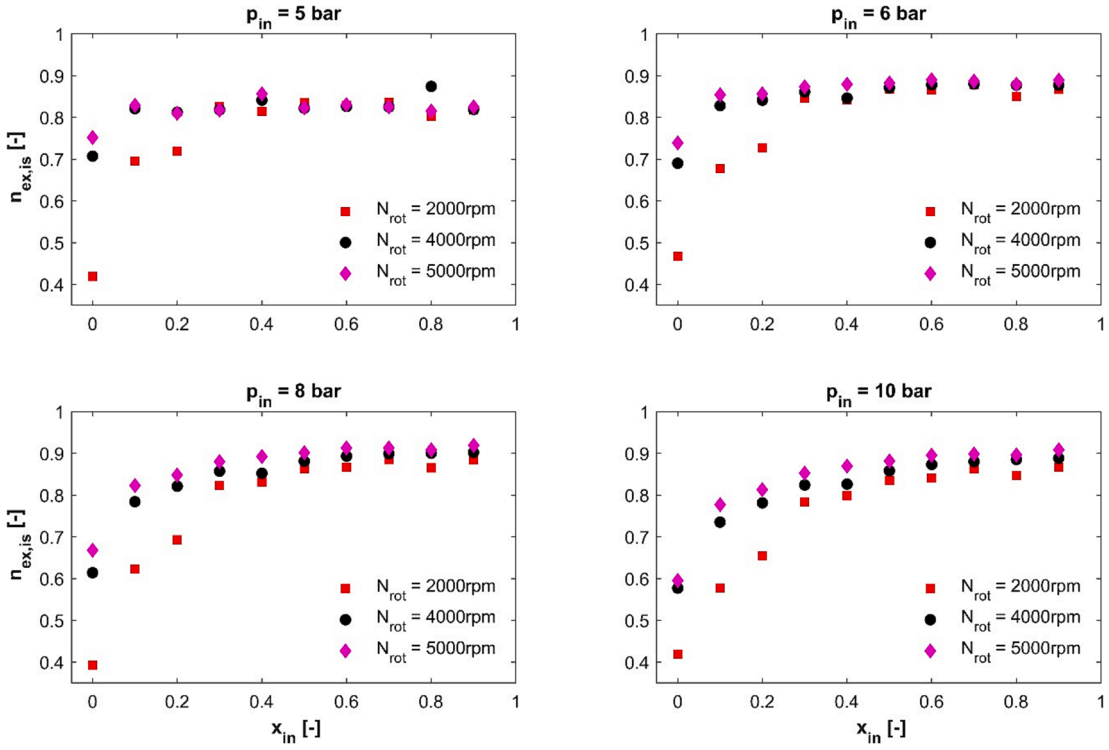

Fig. 8. $\eta_{ex,is}$ [-] as a function of x_{in} and N_{rot} for different values of p_{in}.

series of simulations with varying boundary conditions and R245fa as the WF. Specifically, p_{in}, N_{rot}, and x_{in} vary between 5 and 10 bars, 2000 and 5000 rpm, and 0 and 1, respectively. On the other hand, p_{dis} is kept constant at 1.32 bars, as in the numerical experiments performed by Bianchi et al. [22].

Contours of $\dot{m}_{WF}$ at the p_{in} - N_{rot} plane for different values of x_{in} are presented in Fig. 5. At a given rotational speed of the expander and quality of the two-phase mixture at the suction port, increasing p_{in} leads always to an increase in $\dot{m}_{WF}$. This is attributed to the increase in the displaced mass flowrate $\dot{m}_{ex}$, because of the WF's specific volume reduction (see Eq. (A17) in Appendix A). This mass flow rate increment is more significant, in terms of percentage growth, as x_{in} at the suction

Table 4
Parameters for TFC performance simulations.

Parameter	Description [Units]	Value
WF	Working Fluid [-]	R245fa
HTF	Heat Transfer Fluid [-]	H_2O
CF	Cooling Fluid [-]	H_2O
ΔT_{CF}	Temperature rise of the CF [°C]	10
ΔT_{sub}	WF sub-cooling at condenser [°C]	5
p_{dis}	Condensation pressure of WF [bar]	1.32
PP_{ev}	Pinch point at evaporator [°C]	5
PP_{con}	Pinch point at condenser [°C]	5
$T_{HTF,in}$	HTF inlet temperature [°C]	90 ÷ 110
$\dot{Q}_{ev}$	Heat duty at the evaporator [kW_{th}]	250 ÷ 500
$\dot{m}_{HTF}$	Mass flow rate of the HTF [kg/s]	3
$\eta_{pu,is}$	Pump isentropic efficiency [%]	70 [29]

port increases, because for higher vapor quantities the decrease in the WF's specific volume when pressure increases is steeper.

The filling process of the expander is influenced by N_{rot} and x_{in}. Increasing N_{rot} and reducing x_{in} leads to increased pressure losses at the suction port that reduce the displaced mass flowrate $\dot{m}_{ex}$. Indeed, and from results (not presented graphically herein) derived from indicative numerical experiments, when p_{in} is equal to 7.5 bar and x_{in} is reduced from 0.5 to 0.1 at 5000 rpm, the pressure losses at suction increase from 0.5 to 0.8 bar. Also, for p_{in} equal to 10 bar, x_{in} equal to 0.125, and N_{rot} equal to 2500 rpm, p_{su} obtains the value 9.2 bar, whereas if the rotational speed is increased to 4000 rpm, it becomes equal to 8.5 bar.

In Fig. 6, η_{vol} is plotted versus p_{in} and N_{rot} for x_{in} equal to 0 and 0.4 (note that the evolution of η_{vol} for higher vapor qualities is similar to the one presented for $x_{in} = 0.4$). It is observed that for higher values of x_{in} the expander's filling process is close to optimal, with practically no dependence of η_{vol} on p_{in}. On the other hand, η_{vol} varies slightly as a function of N_{rot}. On the contrary, when vapor quality is low the drop in the volumetric efficiency is significantly higher because the density of the two-phase mixture, which is proportional to the pressure losses of the incompressible WF, is substantially increased.

Concerning the generated power from the expander, contours of $\dot{w}_{sh}$ at the p_{in} - N_{rot} plane for different values of x_{in} are plotted in Fig. 7. Increasing p_{in} and reducing x_{in} for a given rotational speed leads to an increase in $\dot{w}_{sh}$ because the mass flow rate $\dot{m}_{WF}$ through the expander is increased. However, the performance of the two-phase expander must be assessed based on its isentropic efficiency $\eta_{ex,is}$ for different operating conditions, and not only on the generated power. In Fig. 8 $\eta_{ex,is}$ is plotted as a function of x_{in} and N_{rot} for different pressure values p_{in} at the suction port of the expander. Increasing x_{in} improves the performance of the expander because a better match between.

r_v and the WF's volume ratio in the expansion chamber can be achieved, combined with higher volumetric efficiency. For lower vapor qualities at the suction port, the expansion process leads to a sharp increase in the WF's volume ratio that cannot be accommodated smoothly by the expander. In any case, $\eta_{ex,is}$ is maximized when the expander's operating conditions minimize over or under-expansion losses, a trend typically observed in ORC expanders as well. Concluding, x_{in} appears to be the most dominant parameter affecting the performance of the two-phase expander. Increasing x_{in} improves both the filling process and the isentropic efficiency of the expander.

It must be noted that the presented two-phase expansion simulations do not consider friction and heat losses (because of the absence of relevant data for comparison) that could potentially deteriorate significantly the performance of the expander. However, the results presented in this Section indicate how the two-phase expansion model can be utilized by the industry or research community. Following model calibration, simulations may be performed within the range of anticipated operating conditions and the efficiency of the expander can be readily determined. Assuming that the performance of the two-phase expander is not satisfactory at the design point, the model can be utilized to optimize its operation. This can be achieved by investigating the influence of the model parameters on $\eta_{ex,is}$ and η_{vol}, based on a sensitivity analysis, in which their values are modified within an acceptable range.

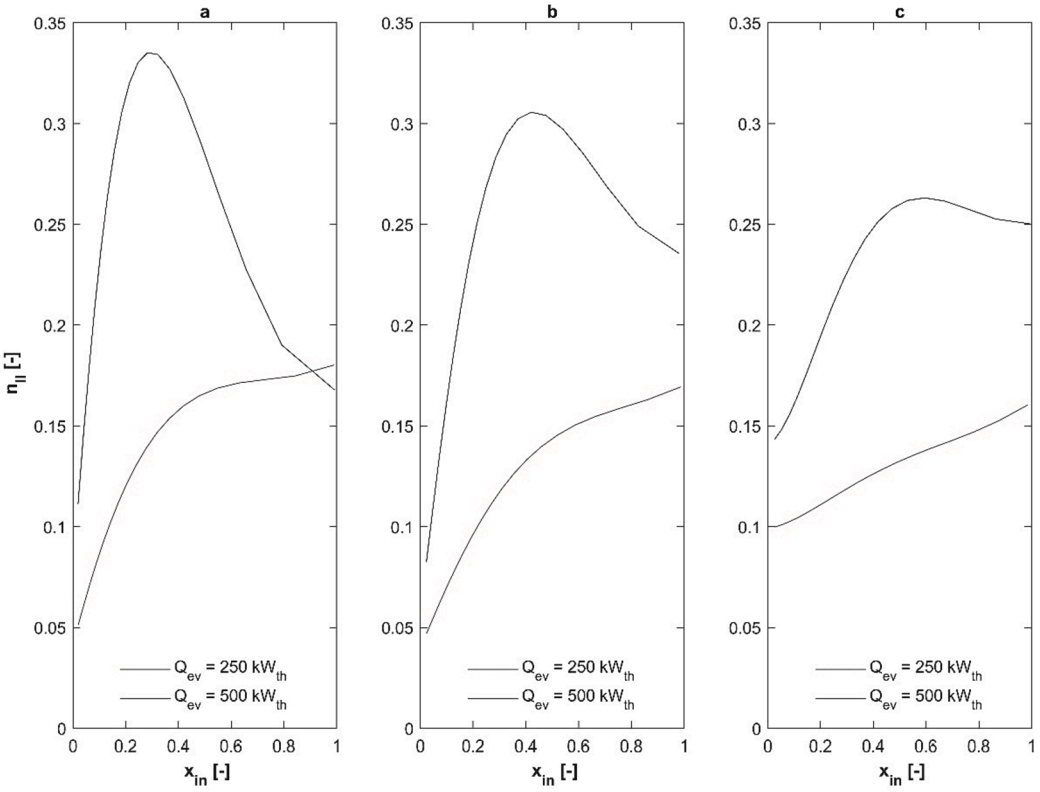

Fig. 9. η_{II} [-] as a function of x_{in} and $\dot{Q}_{ev}$. a) $T_{HTF,in} = 90^oC$, b) $T_{HTF,in} = 100^oC$, c).$T_{HTF,in} = 110^oC$

Table A1
Identified generalized model parameters.

Parameter	Symbol [Units]
Nozzle throat cross-sectional area at suction	A_{in} [m^2]
Nozzle throat cross-sectional area for liquid leakage flows at suction	$A_{l,su}$ [m^2]
Nozzle throat cross-sectional area for vapor leakage flows at suction	$A_{v,su}$ [m^2]
Total swept volume	V_{swept} [m^3]
Nominal thermal conductance between liquid and expander wall at suction	$UA_{l,su,n}$ [W/K]
Nominal WF mass flowrate	$\dot{m}_n$ [kg/s]
Expander built-in volume ratio	r_v [-]
Nozzle throat cross-sectional area for liquid leakage flows during expansion	$A_{l,leak}$ [m^2]
Nozzle throat cross-sectional area for vapor leakage flows during expansion	$A_{v,leak}$ [m^2]
Nominal thermal conductance between liquid and expander wall at discharge	$UA_{l,dis,n}$ [W/K]
Nominal thermal conductance between vapor and expander wall at discharge	$UA_{v,dis,n}$ [W/K]
Mechanical loss torque	τ_{loss} [N-m]
Thermal conductance between expander wall and the ambient	UA_{amb} [W/K]

Thus, geometric characteristics of the expander (such as V_{swept} and r_v) or the insulation of the expander may be improved based on the operating conditions. Furthermore, the performance of a TFC engine integrating the modeled expander can be mapped over a wide range of operating points to assist in the assessment of its potential for practical applications (such a preliminary investigation is presented in Section 4.3).

It must be also pointed out that the two-phase expansion model can be utilized for different WFs (such as state-of-the-art Hydrofluoroolefins) and twin-screw expanders, provided that relevant numerical or experimental data are available for re-calibration. However, for WFs with physical properties similar to the ones of R245fa, based on which the model has been calibrated, preliminary two-phase expansion simulations may be undertaken for expander performance evaluation purposes. An alternative method would be to adjust the WF-related parameters for another fluid and proceed to the expansion modeling, but with reduced accuracy in the obtained results [28]. Finally, the modularity of the algorithm allows for its implementation in different types of volumetric expanders with minor modifications.

4.3. TFC performance

The performance of a TFC engine integrating the modeled two-phase expander for different heat duties $\dot{Q}_{ev}$ at the evaporator, and temperatures $T_{HTF,in}$ of the heat source is investigated by conducting an indicative series of simulations. The parameters used for the TFC simulations, along with their description and units are listed in Table 4.

For given values of $T_{HTF,in}$ and $\dot{Q}_{ev}$, the vapor quality x_{in} at the suction port of the two-phase expander is varied from the saturated liquid to the saturated vapor state, by lowering the pressure p_{ev} at the evaporator, while keeping constant the value of PP_{ev}. In Fig. 9 η_{II} is plotted versus x_{in} for different values of $T_{HTF,in}$ and $\dot{Q}_{ev}$. It can readily be deduced that the energy exploitation efficiency of the TFC engine attains its minimum when x_{in} is equal to 0. This is linked to the rather low isentropic efficiency of the two-phase expander in this region. Therefore, the theoretical optimal match between the heat source and the WF of the original trilateral cycle cannot be achieved by the specific expander for the examined boundary conditions. This condition could be achieved by regulating the operating pressure ratio of the TFC to fit the WF volume ratio to r_v.

For $\dot{Q}_{ev}$ equal to 250 kW$_{th}$, η_{II} increases monotonically within the two-phase region, indicating that the ORC configuration may be the optimal one. The maximum calculated values of η_{th} are equal to 9.33 %, 10.81 %, and 12.35 % for $T_{HTF,in}$ equal to 90, 100, and 110 °C, respectively. On the other hand, for $\dot{Q}_{ev}$ equal to 500 kW$_{th}$ the optimal value of η_{II} is obtained within the two-phase region (x_{in} approximately equal to 0.28, 0.31, and 0.60 for $T_{HTF,in}$ equal to 90, 100, and 110 °C, respectively). Concerning η_{th}, the TFC simulations indicated that the maximum attainable values when $\dot{Q}_{ev}$ is equal to 500 kW$_{th}$ are 8.68 %, 8.69 %, and 10.13 % for $T_{HTF,in}$ equal to 90, 100, and 110 °C, respectively.

The difference in trends of η_{II} for different values of $\dot{Q}_{ev}$ is explained as follows. For a given value of x_{in}, increasing the heat duty $\dot{Q}_{ev}$ leads to lower values of p_{ev}, because of the increased mass flow rate $\dot{m}_{WF}$ of the WF. For the induced pressure ratios when $\dot{Q}_{ev}$ is equal to 500 kW$_{th}$, an optimal match between the WF's volume ratio and r_v can be achieved within the two-phase region, leading to the maximization of $\eta_{ex,is}$, and, therefore, of η_{II}. On the contrary, the optimal pressure ratio for the two-phase mixture cannot be achieved when $\dot{Q}_{ev}$ is equal to 250 kW$_{th}$.

Concluding, the presented numerical results indicate how the developed two-phase expansion model can assist in evaluating the performance of a TFC engine and ameliorating its efficiency. Based on the heat duty at the evaporator and the condensation pressure, TFC power cycle simulations will pinpoint the value of x_{in} that leads to the optimal utilization of the heat source, a condition that will be accomplished when the expander's isentropic efficiency is maximized.

5. Conclusions

In this work, a novel thermodynamic low-order model for the simulation of two-phase expansion in a twin-screw expander was presented. The model applies a robust empirical methodology that is validated by calibrating it against available numerical data from the literature. The methodology may also be applied to other types of two-phase volumetric expanders with minor modifications, because of the generality of the approach. In the paper, detailed results from two-phase expansion simulations are presented to assist in comprehending the operation of the two-phase expander and to identify the factors affecting

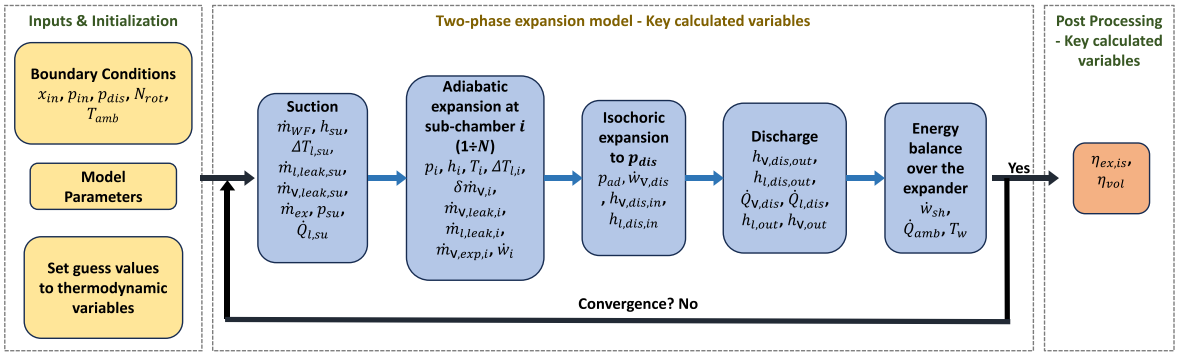

Fig. 10. Two-phase expansion model flowchart.

its efficiency. Thereafter, the potential of the TFC for low-grade heat recovery is preliminarily assessed by investigating the influence of the expander's efficiency on its performance.

The main outcome of the two-phase expansion simulations is that the crucial factor affecting the efficiency of the expander is the quality of the WF at the suction port. Increasing x_{in}, improves substantially $\eta_{ex.is}$, with a steep increase observed in the region around the saturated liquid state. Values as low as 0.40 for $\eta_{ex.is}$ are calculated for x_{in} equal to 0, whereas an increase of its value to up to 0.85 is observed in the two-phase region. For the operating pressure ratios of the two-phase expander studied in this work, the simulations indicate that for x_{in} higher than approximately 0.4, the value of $\eta_{ex.is}$ reaches a practically constant and maximum value. Therefore, for higher amounts of vapor at the onset of expansion, a close to optimal match between the WF's volume ratio and r_v can be achieved. A similar trend is observed for η_{vol}, with significant amelioration of its value as x_{in} increases. Specifically, when the WF is in the saturated liquid state at the suction port of the expander, η_{vol} obtains values in the range of 0.30–0.55. On the other hand, within the two-phase region values as high as 0.90–0.95 are calculated. This is attributed to the reduced pressure losses of the WF at the suction port as its density decreases. Hence, the two-phase expansion simulations indicate that the potential of the ideal trilateral cycle can be realized by expansion machines with very high r_v, that can accommodate both the increased WF flowrates and specific volume increase during expansion.

Since the two-phase expansion simulations indicated that the efficiency of two-phase expansion varies significantly as a function of x_{in}, particular attention should be paid if the two-phase expander will operate across the two-phase region. To highlight this behavior and identify additional efficiency-affecting factors, the performance of a TFC engine integrating the modeled expander was studied for different heat duties at the evaporator and temperatures of the heat source. The results revealed that for a heat transfer rate of 250 kW_{th}, η_{th} and η_{II} increase monotonically within the two-phase region with maximum values reaching 12.35 % and 18 %, respectively. On the other hand, for $\dot{Q}_{ev}$ equal to 500 kW_{th} the maximum efficiency values are obtained within the two-phase region (x_{in} ranging from 0.28 to 0.61, based on the temperature of the heat source), with maximum η_{th} and η_{II} equal to 10.13 % and 33 %, respectively. Thus, as the heat duty at the evaporator increases, the mass flow rate of the WF increases for a given operating pressure ratio and the optimal operating point of the expander may be within the two-phase region. In this case, the TFC could be a competitive alternative to the ORC for low-grade heat recovery.

The developed model will be refined further, and its robustness will be enhanced, by exploiting experimental two-phase expansion data or numerical data from more sophisticated numerical models for its calibration, provided that they become available, and incorporating into the simulations thermal and mechanical losses. Besides investigating the efficiency of a two-phase expander, the presented numerical tool may also be applied to modify the design of a given expander (or optimally design one) by conducting a sensitivity analysis that will identify the optimal values of the model parameters for given operating conditions. Additionally, as presented in this paper, the model can be integrated into power cycle simulations and assist in the techno-economic analysis of a TFC engine for industrial applications.

CRediT authorship contribution statement

Anastasios Skiadopoulos: Investigation, Conceptualization, Methodology, Software, Formal analysis, Writing – original draft, Writing – review & editing. **George Kosmadakis:** Conceptualization, Methodology. **Steven Lecompte:** Supervision. **Michel De Paepe:** Supervision. **Dimitrios Manolakos:** Conceptualization, Methodology, Supervision, Project administration, Funding acquisition, Resources.

Declaration of Competing Interest

The authors declare that they have no known competing financial interests or personal relationships that could have appeared to influence the work reported in this paper.

Data availability

The authors do not have permission to share data.

Acknowledgments

The research work was supported by the Hellenic Foundation for Research and Innovation (H.F.R.I.) under the "First Call for H.F.R.I. Research Projects to support Faculty members and Researchers and the procurement of high-cost research equipment grant" (Project Number: HFRI-FM17-1087, Acronym: SOL-art).

Appendix A. Two-phase expansion modeling

A1. Governing equations

1). Suction

Adiabatic pressure drop

The adiabatic pressure drop is modeled as a fast and isentropic flow of an incompressible fluid through a converging nozzle with a throat cross-sectional area equal to A_{in}. The pressure p_{su} at the end of the process is calculated by application of the Bernoulli equation, as in Eq. (A1)

$$p_{su} = p_{in} - \frac{v_{in}}{2}\left(\frac{\dot{m}_{WF}}{A_{in}}\right)^2 \tag{A1}$$

where v_{in} is the specific volume of the WF, and $\dot{m}_{WF}$ is the total mass flow rate entering the expander. The energy conservation equation for the process is expressed by Eq. (A2)

$$\dot{m}_{WF} h_{in} = \dot{m}_{WF} h_{su} \tag{A2}$$

In Eq. (A2) h_{in} and h_{su} are the specific enthalpies of the mixture at the suction port, and the end of the process, respectively. Because of the pressure drop, the liquid is superheated by $\Delta T_{l,su}$, which is calculated by Eq. (A3)

$$h_{l,su} = h_{l,sat,su} + c_{p_{l,su}} \Delta T_{l,su} \tag{A3}$$

where $h_{l,su}$ and $h_{l,sat,su}$ are the specific enthalpies of the superheated and saturated liquid at p_{su}, respectively, and $c_{p_{l,su}}$ is the specific heat of the liquid

at p_{su}. By applying Eq. (A3) to calculate the specific enthalpy of a superheated liquid, no equations of state for the metastable liquid phase are necessary.

Vaporization at suction

The liquid superheat $\Delta T_{l,su}$ is assumed to drive the vaporization process leading to the pre-expansion of the WF at the suction port. Based on the Interfacial Exchange Model approach, the amount of vapor to be generated is given by Eq. (A4)

$$\delta\dot{m}_{v,su} = \frac{UA_{su}\Delta T_{l,su}}{h_{lv}(p_{su})} \tag{A4}$$

where UA_{su} and $h_{lv}(p_{su})$ are the interfacial thermal conductance and the specific enthalpy of vaporization at p_{su}, respectively.

Leakages at suction

Liquid leakage flow is assumed as isentropic and incompressible through a convergent nozzle of cross-sectional area equal to $A_{l,su}$. Therefore, the liquid leakage flow rate $\dot{m}_{l,leak,su}$ is given by appropriately formulating the Bernoulli equation, as in Eq. (A5)

$$\dot{m}_{l,leak,su} = A_{l,su}\sqrt{2\frac{p_{su}-p_{dis}}{v_{l,su}}} \tag{A5}$$

where $v_{l,su}$ is the specific volume of the saturated liquid at p_{su}.

On the other hand, the leakage flow rate $\dot{m}_{v,leak,su}$ of vapor is modeled as an isentropic flow through a convergent nozzle with a throat cross-sectional area equal to $A_{v,su}$. Thus, $\dot{m}_{v,leak,su}$ is given by Eq. (A6)

$$\dot{m}_{v,leak,su} = \frac{A_{v,su}}{v_{v,thr,su}}\sqrt{2\left(h_{v,su}-h_{v,thr,su}\right)} \tag{A6}$$

In Eq. (A6) $v_{v,thr,su}$ and $h_{v,thr,su}$ are the specific volume and enthalpy at the nozzle throat, respectively, whereas $h_{v,su}$ is the specific enthalpy of saturated vapor at p_{su}. The values of $v_{v,thr,su}$ and $h_{v,thr,su}$ are a function of the pressure $p_{thr,su}$ at the nozzle throat, which is given by Eq. (A7)

$$p_{thr,su} = \max\left(p_{dis}, p_{crit,su}\right) \tag{A7}$$

with $p_{crit,su}$ standing for the critical pressure at the nozzle throat, calculated by Eq. (A8), considering saturated vapor as a perfect gas with a specific heat ratio γ

$$p_{crit,su} = p_{su}\left(\frac{2}{\gamma+1}\right)^{\left(\frac{\gamma}{\gamma-1}\right)} \tag{A8}$$

Liquid isobaric cooling down

The heat transfer rate $\dot{Q}_{l,su}$ from liquid towards the wall of the expander is given by the expression in Eq. (A9)

$$\dot{Q}_{l,su} = UA_{l,su}\left(T_{l,su}-T_w\right) \tag{A9}$$

where $T_{l,su}$ is its temperature after phase change has completed, and T_w is the uniform temperature of a fictitious metal envelope that represents the total metal mass of the expander case and rotating lobes. Moreover, $UA_{l,su}$ is the thermal conductance between the liquid and the expander wall at the suction port. Similar to the approach of Lemort et al. [23] $UA_{l,su}$ is given by Eq. (A10)

$$UA_{l,su} = UA_{l,su,no}\left(\frac{\dot{m}_{WF}}{\dot{m}_{no}}\right)^{0.8} \tag{A10}$$

where $UA_{l,su,no}$ is the liquid nominal thermal conductance corresponding to the WF nominal mass flow rate $\dot{m}_{no}$. This nominal mass flow rate $\dot{m}_n$ is only introduced as a reference for the definition of $UA_{l,su,n}$.

Energy balance at suction

The overall energy balance at the suction port is given by the expression in Eq. (11)

$$\dot{m}_{WF}h_{in} = \dot{m}_{l,ex}h_{l,ex} + \dot{m}_{v,ex}h_{v,su} + \dot{m}_{l,leak,su}h_{l,su} + \dot{m}_{v,leak,su}h_{v,su} + \dot{Q}_{l,su} \tag{A11}$$

where $\dot{m}_{l,ex}$ and $\dot{m}_{v,ex}$ are the total liquid and vapor, respectively, mass flow rates flowing into the expansion chamber. Moreover, $h_{l,ex}$ is the specific enthalpy of the liquid after the filling process has completed. Depending on the vaporization and heat transfer rates at suction, the liquid may be superheated at the end of the filling process, and $h_{l,ex}$ will not be necessarily equal to $h_{l,sat,su}$.

Displaced mass flow rate

The mass conservation for the entire filling process is given by Eq. (A12)

$$\dot{m}_{WF} = \dot{m}_{ex} + \dot{m}_{leak,su} \tag{A12}$$

with the total mass flow rate $\dot{m}_{ex}$ displaced by the expander given by Eq. (A13)

$$\dot{m}_{ex} = \dot{m}_{l,ex} + \dot{m}_{v,ex} \tag{A13}$$

and $\dot{m}_{leak,su}$ the total leakages flow rate at suction, equal to the sum of vapor and liquid leakage flow rates, as in Eq. (A14)

$$\dot{m}_{leak,su} = \dot{m}_{l,leak,su} + \dot{m}_{v,leak,su} \tag{A14}$$

Considering the two phases separately, their mass conservation during the suction process for the liquid and vapor is given by Eqs. (A15) and (A16), respectively

$$\dot{m}_{l,ex} = \dot{m}_{l,WF} - \delta\dot{m}_{v,su} - \dot{m}_{l,leak,su} \tag{A15}$$

$$\dot{m}_{v,ex} = \dot{m}_{v,WF} + \delta\dot{m}_{v,su} - \dot{m}_{v,leak,su} \tag{A16}$$

The displaced mass flow rate $\dot{m}_{ex}$ is also given by Eq. (A17)

$$\dot{m}_{ex} = \frac{N_{rot} V_{swept}}{v_{su}} \tag{A17}$$

where N_{rot}, V_{swept}, and v_{su} represent the rotational speed of the expander, the total swept volume, and the specific volume of the two-phase mixture at the end of suction, respectively.

2). Expansion

Adiabatic expansion to p_{ad} imposed by r_v

A segmental approach is followed, and the expansion chamber volume is divided into N segments that correspond to different rotational angles of the male rotor. The discretization of the expansion chamber into N sub-chambers creates $N+1$ control points, with the first and last corresponding to the end of suction and the end of the adiabatic expansion process, respectively. Sub-chamber i is delimited by control points i and $i+1$. To calculate the values of expansion chamber volume V_i at the control points i $(1 \div N+1)$, the expander's built-in volume ratio r_v is utilized. r_v is given by Eq. (A18)

$$r_v = \frac{V_{ad}}{V_{swept}} \tag{A18}$$

where V_{ad} is the expansion chamber volume at the end of the adiabatic expansion. As a result of the expansion chamber volume discretization, the value of V_i at the control point i $(1 \div N+1)$ is given by Eq. (A19).

$$V_i = V_{swept} + \frac{(i-1)}{N} V_{swept}(r_v - 1) \tag{A19}$$

The sub-chamber i defines a computational control volume, which is considered for the application of the governing equations for both phases. It is assumed that in each sub-chamber the following phenomena take place consecutively.

- Vaporization takes place at control point i, as a result of the locally available liquid superheat
- A fraction of vapor and liquid mass escapes the expansion chamber through leakage paths
- The remaining vapor in the chamber expands, whereas the liquid undergoes an adiabatic pressure drop

At the control point i the pressure of the vapor–liquid mixture is p_i (corresponding to p_{su} when i is equal to 1). The vapor temperature $T_{v,i}$ is equal to the saturation temperature $T_{sat,i}$ at p_i, whereas the liquid temperature $T_{l,i}$ is, in the general case, different from $T_{sat,i}$. Therefore, the liquid superheat $\Delta T_{l,i}$ is given by Eq. (A20)

$$\Delta T_{l,i} = T_{l,i} - T_{v,i} \tag{A20}$$

Applying the Interfacial Exchange Model approach, the mass of vapor $\delta\dot{m}_{v,i}$ to be generated is calculated by Eq. (A21)

$$\delta\dot{m}_{v,i} = \frac{UA_{int,i}\Delta T_{l,i}}{h_{lv}(p_i)} \tag{A21}$$

where $UA_{int,i}$ and $h_{lv}(p_i)$ are the interfacial thermal conductance and the specific enthalpy of vaporization at control point i, respectively. The total vapor mass flow rate $\dot{m}_{v,pc,i}$ increases, and it is now given by Eq. (A22)

$$\dot{m}_{v,pc,i} = \dot{m}_{v,i} + \delta\dot{m}_{v,i} \tag{A22}$$

whereas the total liquid mass flow rate $\dot{m}_{l,pc,i}$ decreases by the same quantity $\delta\dot{m}_{v,i}$, and it is calculated by Eq. (A23)

$$\dot{m}_{l,pc,i} = \dot{m}_{l,i} - \delta\dot{m}_{v,i} \tag{A23}$$

In Eqs. (A22) and (A23) $\dot{m}_{v,i}$ and $\dot{m}_{l,i}$ are the mass flow rates of the vapor and liquid phases, respectively, at control point i before vaporization. The energy balance equation during vaporization is expressed by Eq. (A24)

$$\dot{m}_{l,i}h_{l,i} = \dot{m}_{l,pc,i}h_{l,pc,i} + \delta\dot{m}_{v,i}h_{v,i} \tag{A24}$$

where $h_{l,i}$, $h_{l,pc,i}$, and $h_{v,i}$ are the specific enthalpies of the liquid before vaporization, of the liquid after vaporization, and of the saturated vapor at p_i, respectively.

Vapor leakage flow is considered an isentropic flow through a convergent nozzle with a throat cross-sectional area equal to $A_{v,leak}$. Hence, the vapor leakage mass flow rate $\dot{m}_{v,leak,i}$ through the nozzle is given by Eq. (A25)

$$\dot{m}_{v,leak,i} = \frac{A_{v,leak}}{v_{v,thr,i}} \sqrt{2\left(h_{v,i} - h_{v,thr,i}\right)} \tag{A25}$$

where $v_{v,thr,i}$ and $h_{v,thr,i}$ are the specific volume and enthalpy at the nozzle throat, respectively, and they are calculated based on the pressure $p_{thr,i}$ at the nozzle throat, which is given by Eq. (A26)

$$p_{thr,i} = \max\left(p_{dis}, p_{crit,i}\right) \tag{A26}$$

Similar to the approach followed at the suction port, $p_{crit,i}$ is calculated considering saturated vapor at control point i as an ideal gas.

The liquid leakage flow rate $\dot{m}_{l,leak,i}$ is calculated by considering the isentropic flow of an incompressible fluid through a convergent nozzle of cross-sectional area $A_{l,leak}$, as in Eq. (A27)

$$\dot{m}_{l,leak,i} = A_{l,leak}\sqrt{2\frac{p_i - p_{dis}}{v_{l,i}}} \tag{A27}$$

with $v_{l,i}$ the saturated liquid specific volume at p_i.

The vapor mass flow rate $\dot{m}_{v,exp,i}$ to be expanded is now calculated by Eq. (A28)

$$\dot{m}_{v,exp,i} = \dot{m}_{v,pc,i} - \dot{m}_{v,leak,i} \tag{A28}$$

Assuming that only vapor expansion causes the increase in the expansion chamber volume, the specific volume of $v_{v,i+1}$ of vapor at the control point $i+1$ is calculated by applying Eq. (A29)

$$\dot{m}_{v,exp,i}\left(v_{v,i+1} - v_{v,i}\right) = N_{rot}(V_{i+1} - V_i) \tag{A29}$$

where $v_{v,i}$ is the specific volume of vapor at control point i. Having calculated $v_{v,i+1}$ by applying Eq. (A29), the value of p_{i+1} is readily determined by Eq. (A30)

$$p_{i+1} = p\left(WF, v = v_{v,i+1}, x = 1\right) \tag{A30}$$

Thereafter, the energy balance for the expanding vapor, expressed by Eq. (A31), leads to the calculation of the expansion work $\dot{w}_i$ at sub-chamber i

$$\dot{m}_{v,exp,i}h_{v,i} = \dot{m}_{v,exp,i}h_{v,i+1} + \dot{w}_i \tag{A31}$$

In Eq. (A31) $h_{v,i+1}$ denotes the specific enthalpy of the saturated vapor at p_{i+1}.

On the other hand, the liquid mass flow rate $\dot{m}_{l,exp,i}$ that remains in the expansion chamber is calculated by Eq. (A32)

$$\dot{m}_{l,exp,i} = \dot{m}_{l,pc,i} - \dot{m}_{l,leak,i} \tag{A32}$$

and its energy balance is given by Eq. (A33)

$$\dot{m}_{l,exp,i}h_{l,pc,i} = \dot{m}_{l,exp,i}h_{l,i+1} \tag{A33}$$

By applying Eq. (A33), the specific enthalpy $h_{l,i+1}$ of the liquid at control point $i+1$ may be readily calculated.

The total power $\dot{w}_{exp}$ generated by vapor during the process is calculated by Eq. (A34)

$$\dot{w}_{exp} = \sum_{i=1}^{N}\dot{w}_i \tag{A34}$$

Isochoric expansion to p_{dis}

The possible mismatch between p_{ad}, which corresponds to the calculated pressure at the last control point $N+1$ of the discretized expansion chamber, and p_{dis} is modeled as an adiabatic expansion under constant machine volume for the vapor phase, and an adiabatic pressure drop for the liquid. The power $\dot{w}_{v,dis}$ produced by vapor is calculated by Eq. (A35)

$$\dot{w}_{v,dis} = \dot{m}_{v,ad}v_{v,ad}(p_{ad} - p_{dis}) \tag{A35}$$

with $\dot{m}_{v,ad}$, and $v_{v,ad}$ representing the mass flow rate, and the specific volume of vapor at the end of the adiabatic expansion, respectively. The energy balance for the vapor is given by Eq. (A36)

$$\dot{m}_{v,ad}\left(h_{v,ad} - h_{v,dis,in}\right) = \dot{w}_{v,dis} \tag{A36}$$

In Eq. (A36) $h_{v,ad}$ and $h_{v,dis,in}$ are the specific enthalpies of vapor at the onset and completion of the process, respectively.

On the other hand, the energy balance for the liquid phase is expressed by Eq. (A37)

$$\dot{m}_{l,ad}h_{l,ad} = \dot{m}_{l,ad}h_{l,dis,in} \tag{A37}$$

where $\dot{m}_{l,ad}$ and $h_{l,ad}$ are the liquid mass flow rate and specific enthalpy at the end of the adiabatic expansion process, respectively. Moreover, $h_{l,dis,in}$ is the specific enthalpy of the liquid when the isochoric expansion has completed.

3). Discharge

Adiabatic mixing between leakage flows and expansion chamber outlet

At the beginning of the discharge process, vapor flowing out of the expansion chamber is adiabatically mixed with vapor leakages from the suction port, and the two-phase mixture flowing out of the expansion chamber. The same process takes place for the liquid phase as well. Therefore, the energy balance equation for vapor is formulated as in Eq. (A38)

$$\dot{m}_{v,out}h_{v,dis,out} = \dot{m}_{v,ad}h_{v,dis,in} + \sum_{i=1}^{N}\dot{m}_{v,leak,i}h_{v,i} + \dot{m}_{v,leak,su}h_{v,su} \tag{A38}$$

where $\dot{m}_{v,out}$ and $h_{v,dis,out}$ are the resulting total vapor mass flow rate and specific enthalpy, respectively.

Likewise, for the liquid in Eq. (A39)

$$\dot{m}_{l,out}h_{l,dis,out} = \dot{m}_{l,ad}h_{l,dis} + \sum_{i=1}^{N}\dot{m}_{l,leak,i}h_{l,i} + \dot{m}_{l,leak,su}h_{l,su} \tag{A39}$$

Isobaric heat transfer to the expander wall

The heat transfer rate $\dot{Q}_{v,dis}$ from vapor at the discharge port is given by Eq. (A40)

$$\dot{Q}_{v,dis} = UA_{v,dis}\left(T_{v,dis} - T_w\right) \tag{A40}$$

where $T_{v,dis}$ and $UA_{v,dis}$ are the vapor temperature, and the thermal conductance between vapor and the expander wall, respectively. The energy

balance equation for the vapor phase is expressed by Eq. (A41)

$$\dot{m}_{v,out}h_{v,out} = \dot{m}_{v,dis}h_{v,dis,out} + \dot{Q}_{v,dis} \tag{A41}$$

On the other hand, the liquid heat transfer rate $\dot{Q}_{l,dis}$ towards the expander wall is given by Eq. (A42).

$$\dot{Q}_{l,dis} = UA_{l,dis}\left(T_{l,dis} - T_w\right) \tag{A42}$$

In Eq. (A42) $UA_{l,dis}$ stands for the thermal conductance between the liquid phase and the expander wall at the discharge port, whereas $T_{l,dis}$ is the liquid temperature when the process begins. The energy balance for the liquid is given by Eq. (A43)

$$\dot{m}_{l,out}h_{l,out} = \dot{m}_{l,dis}h_{l,dis,out} + \dot{Q}_{l,dis} \tag{A43}$$

Similar to the approach at the suction port [23], $UA_{v,dis}$ and $UA_{l,dis}$ are given by Eqs. (A44) and (A45), respectively,

$$UA_{v,dis} = UA_{v,dis,no}\left(\frac{\dot{m}_{WF}}{\dot{m}_{no}}\right)^{0.8} \tag{A44}$$

$$UA_{l,dis} = UA_{l,dis,no}\left(\frac{\dot{m}_{WF}}{\dot{m}_{no}}\right)^{0.8} \tag{A45}$$

with $UA_{v,dis,no}$ and $UA_{l,dis,no}$ representing the nominal thermal conductance between the liquid and vapor, respectively, and the expander wall.

4). Mechanical losses

All losses throughout the two-phase expansion process, incorporating friction and bearing losses, are grouped in τ_{loss} that represents an integrated mechanical loss torque [23]. Therefore, mechanical losses $\dot{w}_{loss}$ are given by Eq. (A46)

$$\dot{w}_{loss} = 2\pi N_{rot}\tau_{loss} \tag{A46}$$

5). Energy and heat balance over the expander

The overall energy balance over the two-phase expander, from the suction port to discharge, is given by Eq. (A47)

$$\dot{m}_{WF}h_{in} = \dot{m}_{v,out}h_{v,out} + \dot{m}_{l,out}h_{l,out} + \dot{Q}_{l,su} + \dot{Q}_{l,dis} + \dot{Q}_{v,dis} + \dot{w}_{loss} + \dot{w}_{sh} \tag{A47}$$

where $\dot{w}_{sh}$ is the total shaft power, given by Eq. (A48).

$$\dot{w}_{sh} = \dot{w}_{exp} + \dot{w}_{v,dis} \tag{A48}$$

By introducing the overall thermal conductance UA_{amb} between the expander wall and the ambient, the total heat transfer rate towards the ambient is given by Eq. (A49)

$$\dot{Q}_{amb} = UA_{amb}(T_w - T_{amb}) \tag{A49}$$

with T_{amb} representing the ambient temperature. $\dot{Q}_{amb}$ is assumed to engulf all heat and mechanical friction losses during the expander's operation, as in Eq. (A50)

$$\dot{Q}_{amb} = \dot{Q}_{l,su} + \dot{Q}_{l,dis} + \dot{Q}_{v,dis} + \dot{w}_{loss} \tag{A50}$$

By applying Eq. (A49) the temperature T_w of the metallic envelope is computed [23].

A2. Pinpointing of model parameters

The observation of the governing equations for the two-phase expansion model, presented in SectionA1, leads to the identification of the unknown parameters. This set of parameters can be reduced based on the availability of information concerning the geometrical data of the expander (e.g. built-in volume ratio, swept volume, variation of leakage path areas as a function of the rotation angle of the male rotor), the insulation of the expander's case, or the efficiency of the interfacial heat transfer.

In the present work, aiming to reduce the complexity of the optimization problems, the interfacial thermal conductance values, at suction and expansion as well, are indirectly calculated according to the empirical formula of Miyatake et al. [21], expressed by Eq. (A51), which correlates the flashing efficiency η_f in pure substances with the locally available liquid superheat ΔT

$$\eta_f = \begin{cases} 1 - [1 + 2.5(\Delta T - 1)]^{-1}, \Delta T > 1 \\ 0, \Delta T < 1 \end{cases} \tag{A51}$$

Flashing efficiency measures the actual vaporization rate relative to the one that would result in thermal equilibrium between the two phases. The calculation of the interfacial thermal conductance parameters by utilizing the concept of flashing efficiency is based on preliminary optimization simulations (see Section 4.1 for details about the optimization process) which indicated that their optimized values fit very well with the ones calculated by the empirical formula of Eq. (A51). However, this approach may not be adequate in different two-phase expansion problems, in which case the interfacial thermal conductance parameters must be included in the optimization process. This part will be continuously researched by the authors to verify its limitations. The symbols, physical descriptions, and units in SI of the remaining generalized model parameters are listed in Table A1.

A3. Model flowchart

A simplified flowchart of the two-phase expansion model is presented in Fig. 10. In the flowchart the sequence of the performed calculations in a simulation, along with the key calculated variables, are presented. The boundary conditions for a simulation are the values of x_{in}, p_{in}, p_{dis}, N_{rot}, and T_{amb}. Moreover, in a simulation, the values of the model parameters are known, either as guess values during the optimization procedure (details in Section 4.1) for their calculation or because they have already been determined.

References

[1] 2030 climate & energy framework | Climate Action, (n.d.). https://ec.europa.eu/clima/policies/strategies/2030_en (accessed July 30, 2021).

[2] C. Forman, I.K. Muritala, R. Pardemann, B. Meyer, Estimating the global waste heat potential, Renew. Sustain. Energy Rev. 57 (2016) 1568–1579, https://doi.org/10.1016/j.rser.2015.12.192.

[3] M. Papapetrou, G. Kosmadakis, A. Cipollina, U. La Commare, G. Micale, Industrial waste heat: Estimation of the technically available resource in the EU per industrial sector, temperature level and country, Appl. Therm. Eng. 138 (2018) 207–216, https://doi.org/10.1016/J.APPLTHERMALENG.2018.04.043.

[4] R. Dickes, O. Dumont, R. Daccord, S. Quoilin, V. Lemort, Modelling of organic Rankine cycle power systems in off-design conditions: An experimentally-validated comparative study, Energy 123 (2017) 710–727, https://doi.org/10.1016/J.ENERGY.2017.01.130.

[5] J. Fischer, Comparison of trilateral cycles and organic Rankine cycles, Energy 36 (2011) 6208–6219, https://doi.org/10.1016/J.ENERGY.2011.07.041.

[6] R. DiPippo, Ideal thermal efficiency for geothermal binary plants, Geothermics 36 (2007) 276–285, https://doi.org/10.1016/J.GEOTHERMICS.2007.03.002.

[7] A. Schuster, S. Karellas, R. Aumann, Efficiency optimization potential in supercritical Organic Rankine Cycles, Energy 35 (2010) 1033–1039, https://doi.org/10.1016/J.ENERGY.2009.06.019.

[8] M. Yari, A.S. Mehr, V. Zare, S.M.S. Mahmoudi, M.A. Rosen, Exergoeconomic comparison of TLC (trilateral Rankine cycle), ORC (organic Rankine cycle) and Kalina cycle using a low grade heat source, Energy 83 (2015) 712–722, https://doi.org/10.1016/j.energy.2015.02.080.

[9] G. Bonolo de Campos, C. Bringhenti, A. Traverso, J. Takachi Tomita, Thermoeconomic comparison between the organic flash cycle and the novel organic Rankine flash cycle (ORFC), Energy Convers. Manag. 215 (2020) 112926.

[10] I.K. Smith, Development of the trilateral flash cycle system: Part 1: Fundamental considerations, Proc. Inst. Mech. Eng. Part A J. Power Energy. 207 (1993) 179–194, https://doi.org/10.1243/PIME_PROC_1993_207_032_02.

[11] R.A. Mckay, R.S. Sprankle, Helical rotary screw expander power system (1974). https://api.semanticscholar.org/CorpusID:109308310.

[12] R.F. Steidel, S. Miki, J.E. Flower, Performance characteristics of the lysholm engine as tested for geothermal power applications in the imperial valley, J. Eng. Gas Turbines Power 104 (1982) 231–240, https://doi.org/10.1115/1.3227255.

[13] I.K. Smith, N. Stošić, C.A. Aldis, Development of the trilateral flash cycle system. Part 3: The design of high-efficiency two-phase screw expanders, Proc. Inst. Mech. Eng. Part A J. Power Energy. 210 (1996) 75–92, https://doi.org/10.1243/pime_proc_1996_210_010_02.

[14] B.P. Kliem, Fundamentals of the Two-Phase Screw-Type Engine [Dissertation], Universität Dortmund, 2005.

[15] H. Öhman, P. Lundqvist, Experimental investigation of a Lysholm Turbine operating with superheated, saturated and 2-phase inlet conditions, Appl. Therm. Eng., Pergamon 50 (1) (2013) 1211–1218.

[16] H. Kanno, N. Shikazono, Experimental study on two-phase adiabatic expansion in a reciprocating expander with intake and exhaust processes, Int. J. Heat Mass Transfer 102 (2016) 1004–1011, https://doi.org/10.1016/j.ijheatmasstransfer.2016.06.081.

[17] K.-Y. Lai, Y.-T. Lee, M.-R. Chen, Y.-H. Liu, Comparison of the trilateral flash cycle and Rankine cycle with organic fluid using the pinch point temperature, Entropy 21 (12) (2019) 1197.

[18] A. Baccioli, M. Antonelli, U. Desideri, Technical and economic analysis of organic flash regenerative cycles (OFRCs) for low temperature waste heat recovery, Appl. Energy 199 (2017) 69–87, https://doi.org/10.1016/j.apenergy.2017.04.058.

[19] H. Taniguchi, K. Kudo, W.H. Giedt, I. Park, S. Kumazawa, Analytical and experimental investigation of two-phase flow screw expanders for power generation, J. Eng. Gas Turbines Power 110 (1988) 628–635, https://doi.org/10.1115/1.3240182.

[20] H. Vasuthevan, A. Brümmer, Theoretical investigation of flash vaporisation in a screw expander, IOP Conf. Ser.: Mater. Sci. Eng. 232 (2017) 012077.

[21] O. Miyatake, Y. Koito, K. Tagawa, Y. Maruta, Transient characteristics and performance of a novel desalination system based on heat storage and spray flashing, Desalination 137 (2001) 157–166, https://doi.org/10.1016/S0011-9164(01)00214-4.

[22] G. Bianchi, S. Kennedy, O. Zaher, S.A. Tassou, J. Miller, H. Jouhara, Numerical modeling of a two-phase twin-screw expander for Trilateral Flash Cycle applications, Int. J. Refrig 88 (2018) 248–259, https://doi.org/10.1016/J.IJREFRIG.2018.02.001.

[23] V. Lemort, S. Quoilin, C. Cuevas, J. Lebrun, Testing and modeling a scroll expander integrated into an Organic Rankine Cycle, Appl. Therm. Eng. 29 (2009) 3094–3102, https://doi.org/10.1016/j.applthermaleng.2009.04.013.

[24] M.M. El-Wakil, Nuclear Heat Transport, International Textbook Co., 1971.

[25] P. Downar-Zapolski, Z. Bilicki, L. Bolle, J. Franco, The non-equilibrium relaxation model for one-dimensional flashing liquid flow, Int. J. Multiph. Flow 22 (1996) 473–483, https://doi.org/10.1016/0301-9322(95)00078-X.

[26] Y. Liao, D. Lucas, Computational modelling of flash boiling flows: A literature survey, Int. J. Heat Mass Transf. 111 (2017) 246–265, https://doi.org/10.1016/j.ijheatmasstransfer.2017.03.121.

[27] G.A. Pinhasi, A. Ullmann, A. Dayan, Modeling of flashing two-phase flow, Rev. Chem. Eng. 21 (2005) 133–164, https://doi.org/10.1515/REVCE.2005.21.3-4.133.

[28] G. Kosmadakis, G. Meramveliotakis, S. Karellas, Methods based on a semi-empirical model for simulating scroll compressors with HFC and HFO refrigerants, Open Res. Eur. 1 (2022). https://doi.org/10.12688/OPENRESEUROPE.14313.3.

[29] S. Lecompte, H. Huisseune, M. van den Broek, M. De Paepe, Methodical thermodynamic analysis and regression models of organic Rankine cycle architectures for waste heat recovery, Energy 87 (2015) 60–76, https://doi.org/10.1016/j.energy.2015.04.094.